

Strong Perpendicular Velocity-space Diffusion in Proton Beams Observed by Parker Solar Probe

B. Chandran, D. Larson, K. Paulson, B. Alterman, S. Badman, S. Bale, J. Bonnell, T. Bowen, Thierry Dudok de Wit, J. Verniero, et al.

▶ **To cite this version:**

B. Chandran, D. Larson, K. Paulson, B. Alterman, S. Badman, et al.. Strong Perpendicular Velocity-space Diffusion in Proton Beams Observed by Parker Solar Probe. The Astrophysical Journal, 2022, 924 (2), pp.112. 10.3847/1538-4357/ac36d5 . insu-03578713

HAL Id: insu-03578713

https://insu.hal.science/insu-03578713

Submitted on 17 Feb 2022

HAL is a multi-disciplinary open access archive for the deposit and dissemination of scientific research documents, whether they are published or not. The documents may come from teaching and research institutions in France or abroad, or from public or private research centers.

L'archive ouverte pluridisciplinaire **HAL**, est destinée au dépôt et à la diffusion de documents scientifiques de niveau recherche, publiés ou non, émanant des établissements d'enseignement et de recherche français ou étrangers, des laboratoires publics ou privés.



Distributed under a Creative Commons Attribution 4.0 International License

The Astrophysical Journal, 924:112 (10pp), 2022 January 10 https://doi.org/10.3847/1538-4357/ac36d5
© 2022. The Author(s). Published by the American Astronomical Society.
OPEN ACCESS

Strong Perpendicular Velocity-space Diffusion in Proton Beams Observed by Parker Solar Probe

J. L. Verniero[1], B. D. G. Chandran[2], D. E. Larson[3], K. Paulson[4], B. L. Alterman[5], S. Badman[3,6], S. D. Bale[3,6], J. W. Bonnell[3], T. A. Bowen[3], T. Dudok de Wit[7], J. C. Kasper[4,8], K. G. Klein[9], E. Lichko[9], R. Livi[3], M. D. McManus[3,6], A. Rahmati[3], D. Verscharen[10,11], J. Walters[9], and P. L. Whittlesey[3]
[1] Code 672, NASA, Goddard Space Flight Center, Greenbelt, MD 20771, USA;
[2] Physics Department, University of New Hampshire, Durham NH 03824, USA
[3] Space Sciences Laboratory, University of California, Berkeley, CA 94720, USA
[4] Smithsonian Astrophysical Observatory, Cambridge, MA 02138, USA
[5] Space Science and Engineering, Southwest Research Institute, San Antonio, TX 78238, USA
[6] Physics Department, University of California, Berkeley, CA 94720, USA
[7] LPC2E, CNRS and University of Orléans, Orléans, France
[8] Climate and Space Sciences and Engineering, University of Michigan, Ann Arbor, MI 48109, USA
[9] Lunar and Planetary Laboratory, University of Arizona, Tucson, AZ 85721, USA
[10] Mullard Space Science Laboratory, University College London, Dorking, RH5 6NT, UK
[11] Space Science Center, University of New Hampshire, Durham, NH 03824, USA
Received 2021 August 17; revised 2021 October 17; accepted 2021 November 3; published 2022 January 18

Abstract

The SWEAP instrument suite on Parker Solar Probe (PSP) has detected numerous proton beams associated with coherent, circularly polarized, ion-scale waves observed by PSP's FIELDS instrument suite. Measurements during PSP Encounters 4−8 revealed pronounced complex shapes in the proton velocity distribution functions (VDFs), in which the tip of the beam undergoes strong perpendicular diffusion, resulting in VDF level contours that resemble a "hammerhead." We refer to these proton beams, with their attendant "hammerhead" features, as the ion strahl. We present an example of these observations occurring simultaneously with a 7 hr ion-scale wave storm and show results from a preliminary attempt at quantifying the occurrence of ion-strahl broadening through three-component ion VDF fitting. We also provide a possible explanation of the ion perpendicular scattering based on quasilinear theory and the resonant scattering of beam ions by parallel-propagating, right circularly polarized, fast magnetosonic/whistler waves.

Unified Astronomy Thesaurus concepts: Space plasmas (1544); Alfven waves (23); Solar wind (1534)

1. Introduction

Parker Solar Probe (PSP; Fox et al. 2016) is the nearest human-made object to the Sun, making unprecedented observations of solar wind plasma and electromagnetic fields with every orbit. Prior to PSP, Helios was the spacecraft that had approached closest to the Sun, reaching a heliocentric distance $r \simeq 60\,R_\odot$ or $\simeq$0.3 au. A series of Venus flybys is repeatedly modifying PSP's orbit, reducing the heliocentric distance of PSP's perihelion. PSP's most recent ninth perihelion on 2021 August 09 is at $r \approx 16\,R_\odot$. Within a few years, PSP will reach heliocentric distances just under $10\,R_\odot$. In this paper, we present new PSP observations of proton beams that undergo strong velocity-space diffusion perpendicular to the magnetic field, as well as a theoretical model that explains the shapes of the observed velocity distribution functions (VDFs).

Ion beams in the solar wind at $r > 0.3$ au have been studied extensively over the past five decades (Feldman et al. 1973, 1974; Marsch et al. 1982; Marsch & Livi 1987; Neugebauer et al. 1996; Steinberg et al. 1996; Kasper et al. 2006; Podesta & Gary 2011; Alterman et al. 2018; Klein et al. 2018; Ďurovcová et al. 2019). These nonthermal features in the ion VDFs arise in part because of the nearly collisionless nature of the solar wind. The free energy carried by the beams can drive plasma instabilities and provide an important source of plasma heating in the solar wind (Daughton & Gary 1998; Hu & Habbal 1999; Gary et al. 2000; Marsch 2006; Maneva et al. 2013; Verscharen & Chandran 2013; Verscharen et al. 2013b, 2015). PSP's near-Sun observations provide unique insight at distances $r < 0.3$ au, where beams may be generated.

The secondary proton beam population in VDFs has now been recognized to play as significant a role in energy transfer in the inner heliosphere as the core proton population. Joint observations by PSP's Solar Wind Electrons Alphas and Protons (SWEAP; Kasper et al. 2016) and FIELDS (Bale et al. 2016) instrument suites show the presence of ubiquitous proton beams concurrent with ion-scale waves (Bale et al. 2019; Bowen et al. 2020a; Verniero et al. 2020; Klein et al. 2021). PSP's first perihelion encounter with the Sun revealed a diversity of stream characteristics in the near-Sun solar wind, including large-amplitude Alfvénic "switchbacks" and intervening "quiescent" periods of a near-radial magnetic field (Bale et al. 2019). The quiescent solar wind in Encounters 4−5 illuminated striking patterns between features in the ion VDFs and wave activity. In particular, the proton beam tended to broaden (perpendicular to the magnetic field) over a relatively narrow energy range during periods of coherent ion-scale waves that are right circularly polarized in the spacecraft frame, producing VDFs with level contours with a "hammerhead" shape. The proton VDF populations that lie outside the core population contribute to the main asymmetries leading to

Original content from this work may be used under the terms of the Creative Commons Attribution 4.0 licence. Any further distribution of this work must maintain attribution to the author(s) and the title of the work, journal citation and DOI.

energy transfer. Since these particles carry information regarding ion heat flux, we therefore define the *ion strahl* as the superposition of the narrow field-aligned beam population and the perpendicularly broadened hammerhead population.

In Section 2, we describe a procedure for modeling the ion VDFs as a superposition of three particle populations: a core, a beam of nearly field-aligned particles, and a broadened "hammerhead" population. Using this procedure, we explore correlations between different properties of the hammerhead particles, as well as the association between the prevalence of hammerhead particles and the energy density of right circularly polarized waves at the ion scale. In Section 3, we develop a theoretical model for explaining the shapes of the hammerhead VDFs observed by PSP, and we test this model by comparing its predictions with PSP observations. We present our conclusions in Section 4.

2. Observations: The Hammerhead Feature as a New Asymmetry in Proton VDFs

Here, we describe the PSP observations and methods used for data analysis regarding the prevalence of the ion-strahl broadening simultaneous with ion-scale waves. We combine measurements from both the Solar Wind Electrons Alphas and Protons (SWEAP; Kasper et al. 2016) and FIELDS (Bale et al. 2016) instrument suite. SWEAP combines measurements from a Sun-pointed Faraday cup (FC) called the Solar Probe Cup (SPC; Case et al. 2020) with three top-hat electrostatic analyzers (ESAs) collectively called Solar Probe ANalyzers (SPAN), one that measures ions (SPAN-I Livi et al. 2021) and two that measure electrons (Whittlesey et al. 2020, SPAN-e). While PSP's heat shield partially obscures the SPAN fields of view (FOVs), the joint SPAN-SPC FOVs cover the full sky.

This paper primarily uses SPAN-I 3D measurements of ion VDFs, resolved in $(E,\ \theta,\ \phi) = (\text{energy, elevation, azimuth})$ phase space. The FOV limitations for SPAN-I are carefully considered when choosing appropriate time periods for optimal ion VDF analysis. For the observations described in this section, we use survey SPAN-I data at 7 s cadence from PSP's fourth perihelion around the Sun (Encounter 4). The electromagnetic wave activity is analyzed using the FIELDS instrument, using the highest resolution magnetometer data ($\approx$293 samples s^{-1}) sufficient to capture ion-scale dynamics in the narrow wave frequency band observed between 1 and 7 Hz in the electromagnetic fields data. Following the methodology in Torrence & Compo (1998), Bowen et al. (2020a), Verniero et al. (2020), we extract spacecraft frame wave power and polarization properties of the electromagnetic waves by applying a Morlet wavelet transform to the FIELDS magnetometer data.

Encounter 4 revealed novel complexities in the SPAN-I measured VDFs compared to the ones observed in Encounter 2 (see Figure 2 of Verniero et al. 2020). Figure 1(a) shows an example of these new complex proton VDFs displaying the three core, beam, and hammerhead populations circled in orange, blue, and gray, respectively. The VDF was collapsed onto the θ-plane in $(v_r,\ v_z)$ SPAN-I instrument coordinates, where $v_r = v_x^2 + v_y^2$. The black arrow represents the magnetic field direction rotated in the SPAN-I instrument frame, where the length is the Alfvén speed v_A and the head is placed at the solar wind velocity. The extra asymmetry represented by the hammerhead population (which lies perpendicular to the magnetic field) was first noticed during a 7 hr period of quiescent solar wind accompanied by right-hand (RH) polarized ion-scale waves at $r = 28\,R_\odot$ in Encounter 4, as shown in Figures 1(b)−(e). Displayed is the FIELDS magnetometer observed (b) magnetic field $\boldsymbol{B}$ in RTN coordinates, (c) a wavelet spectrogram of $\boldsymbol{B}$, and (d) perpendicular polarization (red = right-handed in the spacecraft frame, blue = left-handed). During this interval, the proton gyrofrequency was ≈ 1.6 Hz, so the narrowband wave power and polarization from Figures 1(c) and (d), as measured in the spacecraft frame, occur at the proton gyrofrequency scale. Doppler shifting the wave frequencies from the spacecraft to the plasma frame is nontrivial in this interval since the solar wind Mach number was close to unity. Shown in Figure 1(e) is the SPAN-I measured temperature anisotropy $(T_\perp/T_\parallel)$ obtained by the plasma moments of the total proton VDF. Note that we do not obtain this value by diagonalizing the temperature tensor, because SPAN-I's obscured FOV and the resulting partial moments introduce systematic errors. Instead, $\boldsymbol{B}$ is first rotated to the SPAN-I instrument frame and we then extract the perpendicular and parallel components of the temperature tensor with respect to $\boldsymbol{B}$. Note that the presence of the large beam causes $(T_\perp/T_\parallel) < 1$ when only considering the moments of the ion VDF. As discussed in Klein et al. (2021), the fits of the proton VDFs hold more information on the nature of wave −particle energy transfer at kinetic scales.

Over the 7 hr period shown in Figures 1(b)–(e), we performed a triple bi-Maxwellian fit to the VDFs as a rudimentary approach to quantifying the observed tertiary population representing the proton particles participating in perpendicular phase-space diffusion, exhibiting a hammerhead feature. Standard Levenberg−Marquardt fits (Levenberg 1944; Marquardt 1963) were applied to the L2 SPAN-I data; each portion of the proton VDF—core (p1), beam (p2), and hammerhead (p3)—is assigned to a bi-Maxwellian Gaussian function, $f_{\rm pi}|_{(i=1,2,3)}$, that extracts the physical plasma parameters of density $n_{\rm pi}$, velocity $\boldsymbol{v}_{\rm pi}$, and anisotropic temperature $(T_\perp,\ T_\parallel)_{\rm pi}$. Similar to Alterman et al. (2018), the core population f_{p1} is first fitted with a 3D velocity $(v_x,\ v_y,\ v_z)_{p1}$. The other two populations, f_{p2} and f_{p3}, are assumed to be moving parallel to the magnetic field and fitted to a 1D drift velocity $(v_{\rm drift})_{\rm pi}$ relative to the core population. This procedure leads to 14 fitting parameters that can vary to obtain the best fit, up to physically reasonable constraints. First, the initial guess of each fitting parameter did not depend on the previous one, but rather was based on a reasonable fraction of the SPAN-I moments of density $\tilde{n}$, velocity $\tilde{\mathbf{v}}$, and temperature $\tilde{T}$. Next, the parameters $n_{\rm pi}$ and $(T_\perp/T_\parallel)_{\rm pi}$ for each population were constrained to be positive definite while not exceeding $3\tilde{n}$ and $10\tilde{T}$, respectively. Since the magnetic field points inwards in the SPAN-I instrument frame (see black arrow in Figure 1(a)), velocities have a negative sign, so we constrain $(v_{\rm drift})_{\rm pi}$ between $\pm 3\tilde{v}_x$ (since $\tilde{v}_x$ is nearly radial) . From Figure 1(a), we notice that the hammerhead population (gray) exhibits an oblong shape corresponding to a large temperature anisotropy, $(T_\perp/T_\parallel)_{p3}$. To ensure a robust fit convergence, we additionally imposed a threshold $(T_\perp/T_\parallel)_{p1,2}$ of 6 for the core and beam populations and a threshold $(T_\perp/T_\parallel)_{p3}$ of 10 for the hammerhead population. If a given VDF fit exceeds these parameters, then it is discarded.

Figure 2 displays a preliminary occurrence rate quantification of the hammerhead population during the 7 hr ion-scale wave storm shown in Figures 1(b)–(e), and consequently a possible measure related to perpendicular velocity-space

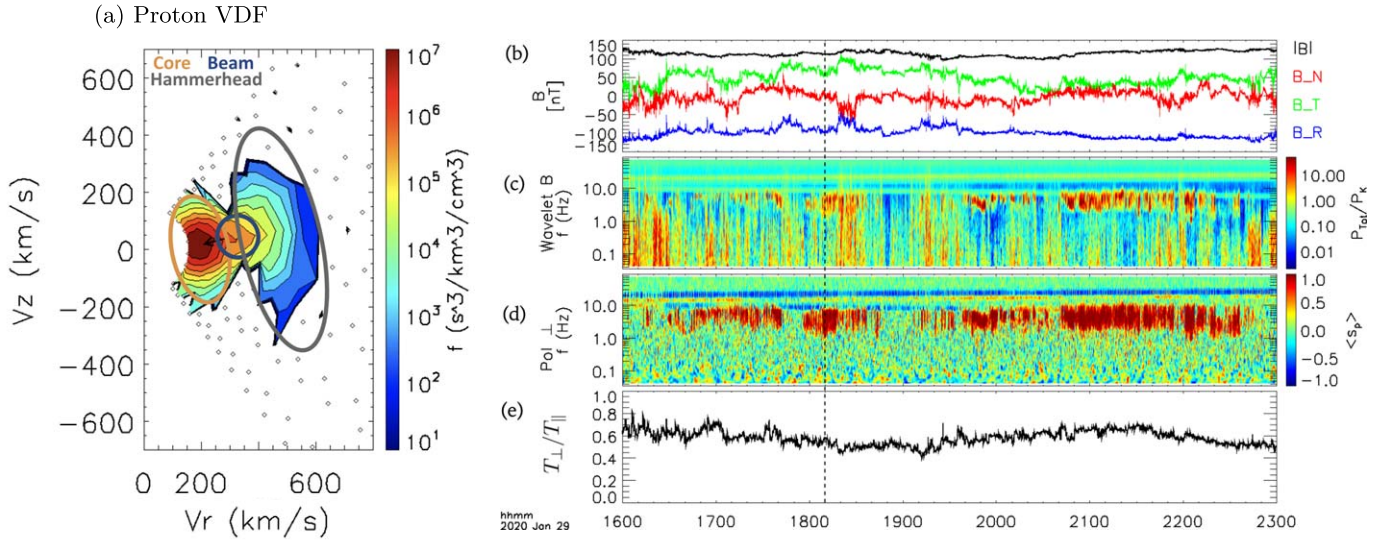


Figure 1. Left: (a) example proton VDF in SPAN-I instrument coordinates during E4 quiescent solar wind period at vertical dashed black line shown on the right. The core, beam, and hammerhead populations are circled in orange, blue, and gray, respectively. The VDF shown was collapsed onto the θ-plane in (v_r, v_z) SPAN-I instrument coordinates, where $v_r = \sqrt{v_x^2 + v_y^2}$. The black arrow indicates the direction of the magnetic field, rotated to SPAN-I instrument coordinates; the head of the arrow is placed at the solar wind velocity, with length representing the local Alfvén speed. Right: the FIELDS magnetometer observations show (b) $\boldsymbol{B}$ in RTN coordinates, (c) a wavelet spectrogram of $\boldsymbol{B}$ (with color scale as total power $P_{\rm tot}$ normalized by background $k^{(-5/3)}$ P_k power), and (d) the perpendicular polarization of $\boldsymbol{B}$ (red = RH, blue = LH in spacecraft frame). Panel (e) shows the SPAN-I measured temperature anisotropy, $T_\perp/T_\parallel$.

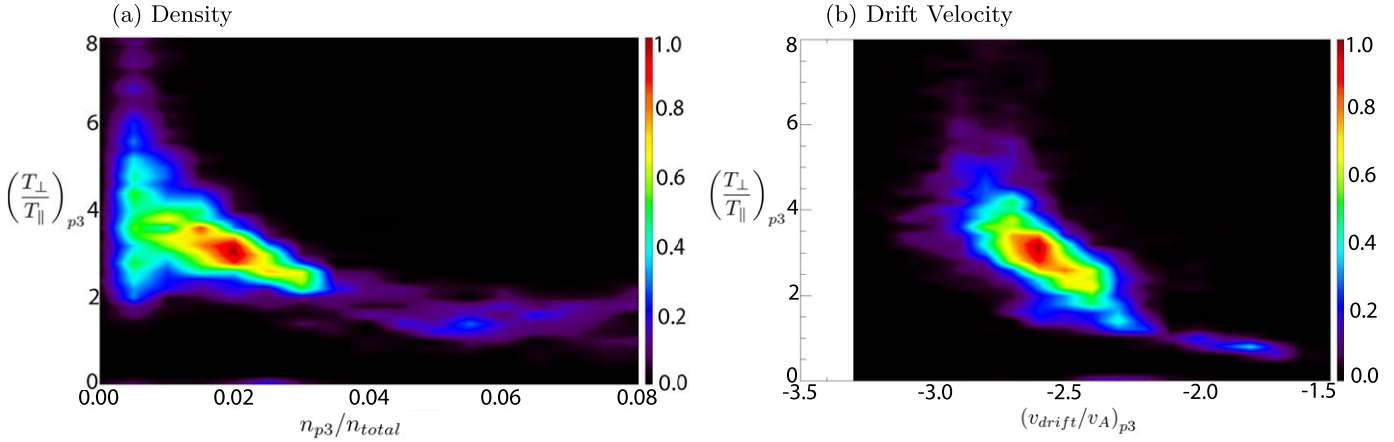


Figure 2. Initial characterization of the hammerhead population through trends of $(T_\perp/T_\parallel)_{p3}$ vs. (a) fractional density and (b) relative drift velocity to the core population, normalized by the local Alfvén speed. Note that since the magnetic field vector points inwards in the SPAN-I instrument frame (see black arrow in Figure 1(a)), velocities have a negative sign during this time period. The color bar on each plot represents the number of fits, normalized by the total.

diffusion strength. We found that $(T_\perp/T_\parallel)_{p3}$ had a mean value of ≈2.5. Figure 2 shows that the hammerhead population was (a) ≈2% of the total proton density and (b) drifting ≈2.5v_A relative to the core population (a negative drift velocity is displayed since the magnetic field is pointing inwards in the SPAN-I instrument frame). From Figure 2(a), we see that $(T_\perp/T_\parallel)_{p3}$ is asymptotic to 1 starting at ≈4%. This suggests that there may be stronger perpendicular diffusion when the hammerhead density is less than 4% of the total proton density; after this threshold, the hammerhead population relaxes toward isotropy and is indistinguishable from the beam population. This maximum density could also be a threshold for the hammerhead population to diffuse into other portions of phase space.

During the 7 hr ion-scale wave storm period displayed in Figures 1(b)–(e), the most intense enhancement of ion-scale wave power activity occurred during 2020 January 29 20:40:00 −21:30:00. Figure 3(a) displays the integrated RH wave power over the ion-scale frequency range of 0.1–9 Hz during this time period. Panels Figures 3(b)–(d) show the three-component fits of temperature anisotropy, drift velocity, and density, respectively. One can notice from Figure 3(b) that at around 2020 January 29 20:20:00, the value of $(T_\perp/T_\parallel)_{p3}$ doubled from ≈1.5 to 3. This is also concurrent with the period of enhanced integrated RH wave power in Figure 3(a). At time $t1$, indicated by the vertical black dashed black line, the wave activity decreased, and $(T_\perp/T_\parallel)_{p3}$ decreased to ≈1.3. As shown by Figure 4(a), the proton VDF does not display a hammerhead feature at $t1$, and the VDF appears more isotropized. By contrast, once the RH wave activity enhances at $t2$, we see from Figure 4(b) that the hammerhead feature in the VDF is more pronounced and follows the black dashed contour arcs. The nature of these predicted curves is explained in Section 3. During the enhanced ion-scale wave period of 2020 January 29 20:40:00−21:30:00, Figure 3(b) shows that $(T_\perp/T_\parallel)_{p3}$ increased again, with a mean value of ≈3.7 and fluctuations up to ≈8. Thus, these preliminary fits suggest that enhanced ion-scale RH

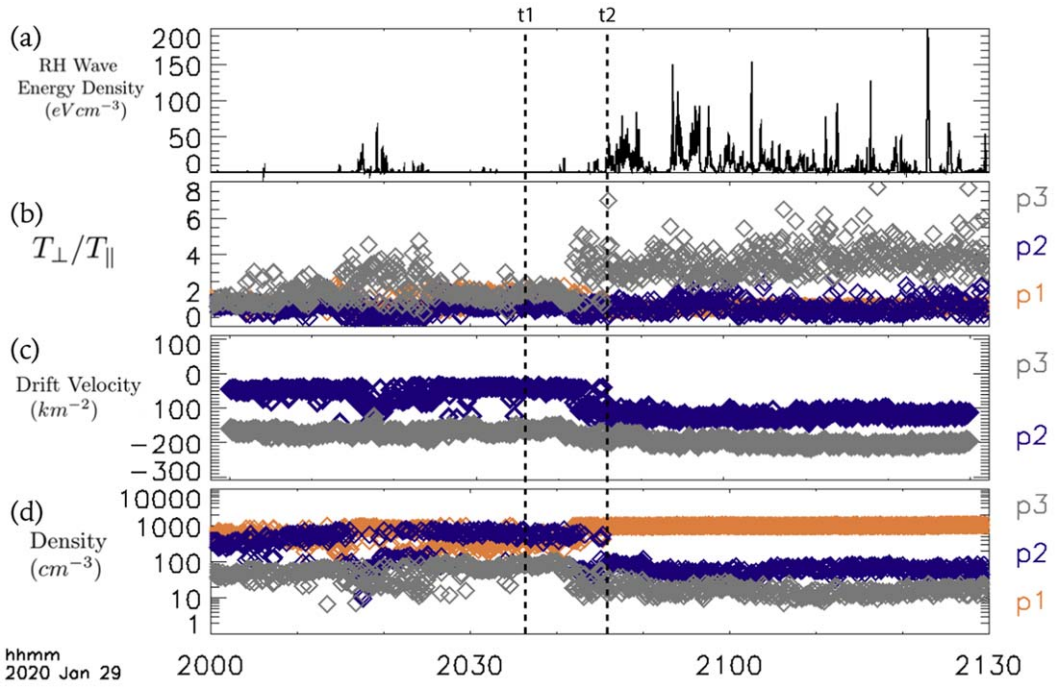


Figure 3. Period of intense wave enhancement showing (a) integrated right-handed wave power over 0.1–9 Hz, (2) temperature anisotropy fits of beam (blue) and hammerhead (gray), (3) drift velocity fits of beam (blue) and hammerhead (gray) with respect to the core, and (4) density fits of core (orange), beam (blue), and hammerhead (gray).

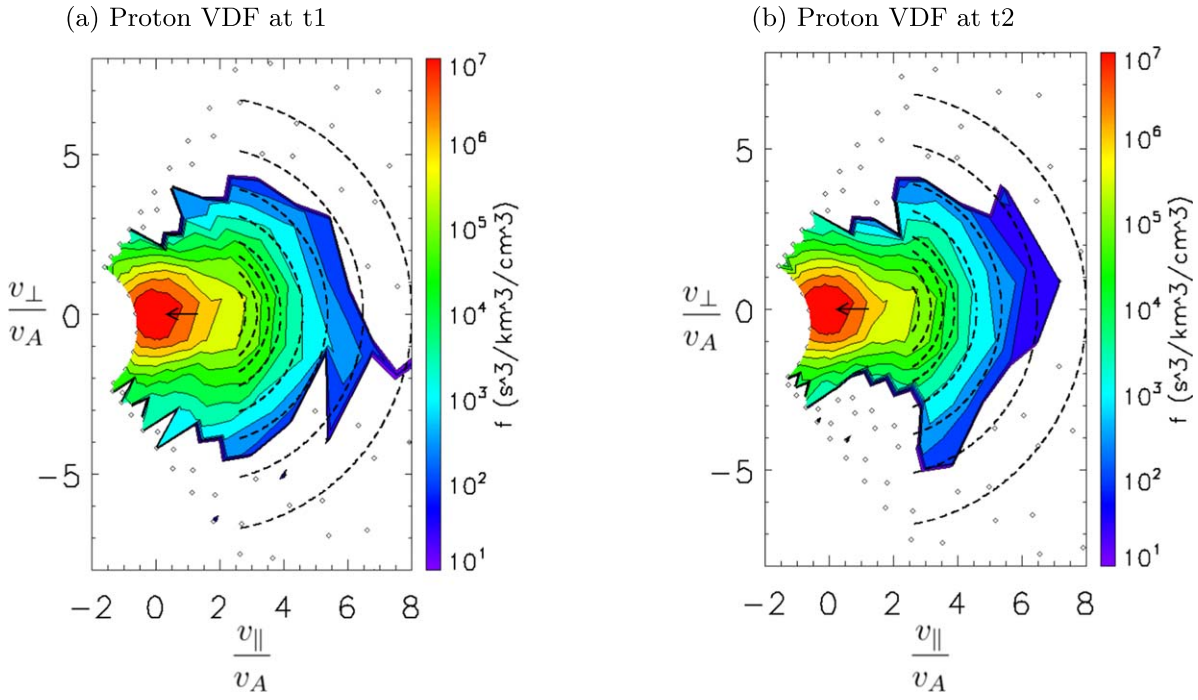


Figure 4. Perpendicular velocity-space diffusion in proton VDFs during period of intense wave enhancement shown in Figure 3. Panels (a) and (b) shows the VDFs in magnetic field-aligned coordinates at $t1$ and $t2$, respectively, indicated by the dashed black lines in Figure 3. The black arrow in each panel indicates the direction of the magnetic field, rotated to SPAN-I instrument coordinates; the head of the arrow is placed at the solar wind velocity, with length representing the local Alfvén speed.

circularly polarized wave activity may be associated with the occurrence rate of the hammerhead feature in the proton VDFs.

Figure 3(c) also shows that the drift velocity of the hammerhead population (relative to the core) increased by $0.5v_A$ from before $t1$ and after $t2$. The observed increase in drift velocity for both the beam and hammerhead populations after $t2$ demonstrates that the overall proton strahl drift is coincident with the enhanced RH ion-scale wave power. One also notices from Figure 3(d) that after $t2$, the density of both the beam (blue) and hammerhead (orange) population decreased, while the core (red) density increased. This may be a consequence of the proton VDF fitting procedure. For example,

before $t2$, when the temperature anisotropy is small, the distinction between $p2$ and $p3$ is less significant. Assuming both $p2$ and $p3$ have substantial drift velocities, both $p2$ and $p3$ can be considered part of the "beam," as seen in Figure 4(a). As a consequence, a large temperature anisotropy for $p3$ is thus a necessary condition in order diagnose the presence of a hammerhead feature. Note that the preceding argument may also explain the density cutoff from Figure 2(a). Within the subset of the data with large $(T_\perp/T_\parallel)_{p3}$, the density of $p3$ could determine the strength of the hammerhead, and subsequently a more quantitative measure of the velocity-space diffusion signature. But, for a binary diagnostic for the hammerhead occurrence rate, we find that $(T_\perp/T_\parallel)_{p3}$ is optimal.

As more evidence that these hammerhead features are concurrent with the RH ion-scale wave storm enhancement, we note that in the period 2020 January 29 16:00:00−23:00:00 where the hammerheads are seen, the peak wave power appears at ≈4.198 Hz. At and around this frequency, the degree of circular polarization was ≈0.722. The degree of circular polarization at 4.198 Hz frequency computed over the whole day was ≈0.056, yielding a ratio of ≈12.8. Thus, these complex asymmetries in the SPAN-I proton VDFs suggest they are associated with RH ion-scale waves.

Motivated by the enhanced levels of right circularly polarized, ion-scale waves during this hammerhead event, we explore in the next section a theoretical model for the origin of hammerhead features that relies on resonant interactions between beam ions and right circularly polarized ion-scale waves.

3. Theory: How Resonant Interactions between Protons and Fast Magnetosonic/Whistler Waves Generate Hammerhead Features in Proton VDFs

As mentioned in the Introduction, particle beams provide a source of free energy that can cause different plasma waves to become unstable. The resonant interaction between the growing waves and the beam particles cause the particles to diffuse in velocity space. This diffusion drives the particle distribution toward a marginally stable state; afterward, the wave growth halts. The isosurfaces in velocity space along which the particle distribution function f is constant in this marginally stable state are referred to as "kinetic shells" (Isenberg et al. 2001). This relaxation toward a marginally stable state results in deceleration and perpendicular heating of the beam ions. The ions lose more energy through deceleration than they gain via perpendicular heating (see Figure 8), and the net energy lost by the beam ions is transferred to the growing fast magnetosonic/whistler (FM/W) waves. In this section, we explain in detail how this process works for ion beams interacting with parallel-propagating FM/W waves. A general solution to this problem was given by Isenberg & Lee (1996), who presented detailed analytic results for the case in which the FM/W waves are described by the cold-plasma dispersion relation. We reproduce parts of their solution here and numerically compute the shape of the kinetic shells for the case in which the FM/W waves are described by the hot-plasma dispersion relation, which is more relevant to the inner heliospheric conditions sampled by PSP.

As alluded to in the previous paragraph, we confine our discussion to the "slab-symmetric" case in which the wavevector is parallel to the background magnetic field $\boldsymbol{B}_0$, assumed in the z direction:

$$\boldsymbol{B}_0 = B_0\hat{\boldsymbol{z}}. \tag{1}$$

Although we consider the interaction of FM/W waves with proton beams, we neglect these beams as well as all heavy ions when determining the dispersion relation of the waves. For the mathematical expressions that follow, we work in the reference frame in which the proton bulk velocity vanishes. We write the FM/W dispersion relation in the form

$$y = F(x), \tag{2}$$

where

$$y = \omega/\Omega_\mathrm{p} \qquad x = k_z v_\mathrm{A}/\Omega_\mathrm{p}. \tag{3}$$

Here, ω is the wave frequency, k_z is the component of the wavevector along $\boldsymbol{B}_0$ (which is the only nonvanishing wavevector component in our analysis), $\Omega_\mathrm{p} = qB/m_\mathrm{p}$ is the proton cyclotron frequency, and $v_\mathrm{A} = B\Big/\sqrt{4\pi i n_\mathrm{p} m_\mathrm{p}}$ is the Alfvén speed. In the cold-plasma approximation for a proton-electron plasma, $F(x)$ is given by

$$F(x) = \frac{x^2}{2}\left(1 + \sqrt{1 + \frac{4}{x^2}}\right) \quad \text{(cold plasma)}, \tag{4}$$

where ω is assumed to be much less than the electron cyclotron frequency.

Waves and ions interact resonantly only when they satisfy the resonance condition

$$\omega - k_z v_z = n\Omega, \tag{5}$$

where v_z is the component of the particle velocity along $\boldsymbol{B}_0$, Ω is the ion cyclotron frequency, and n is any integer. For the present right-handed and parallel FM/W waves under consideration, $n = -1$. The left-hand side of Equation (5) is the wave frequency Doppler shifted into the reference frame that moves along $\boldsymbol{B}_0$ at the same velocity as the ion, which we call the "parallel co-moving frame."

For concreteness, we take ω to be positive. (This entails no loss of generality; negative frequencies can be accommodated by flipping the sign of k_z in the discussion to follow.) We assume that the beam ions satisfy $v_z > 0$. (Again this implies no loss of generality.) We then restrict our attention to FM/W waves traveling in the $+z$ direction, i.e., with positive values of ω/k_z, which amounts to taking $k_z > 0$, given our assumption that $\omega > 0$. Interactions between FM/W waves and beam ions propagating in the opposite direction can occur, but they generally give rise to particle energization and hence wave damping, and are thus not relevant to the scenario we are exploring in this section, in which resonant wave−particle interactions amplify FM/W waves while decelerating beam ions (see Verscharen et al. 2013a, for a further discussion).

Parallel-propagating, right circularly polarized FM/W waves with $\omega > 0$ resonate with ions only via the $n = -1$ resonance in Equation (5); (Stix 1992; Tsurutani & Lakhina 1997). To understand the importance of the $n = -1$ resonance for ion −FM/W interactions, it is useful to consider a 3D coordinate system (x, y, z) transformed to $(E_x(z), E_y(z), z)$ space, where electric field components E_x and E_y are evaluated as functions of z along some particular field line of $\boldsymbol{B}_0$. This resulting curve is a helix centered on the z axis, which we refer to as the "electric field corkscrew." The tilt of this corkscrew is

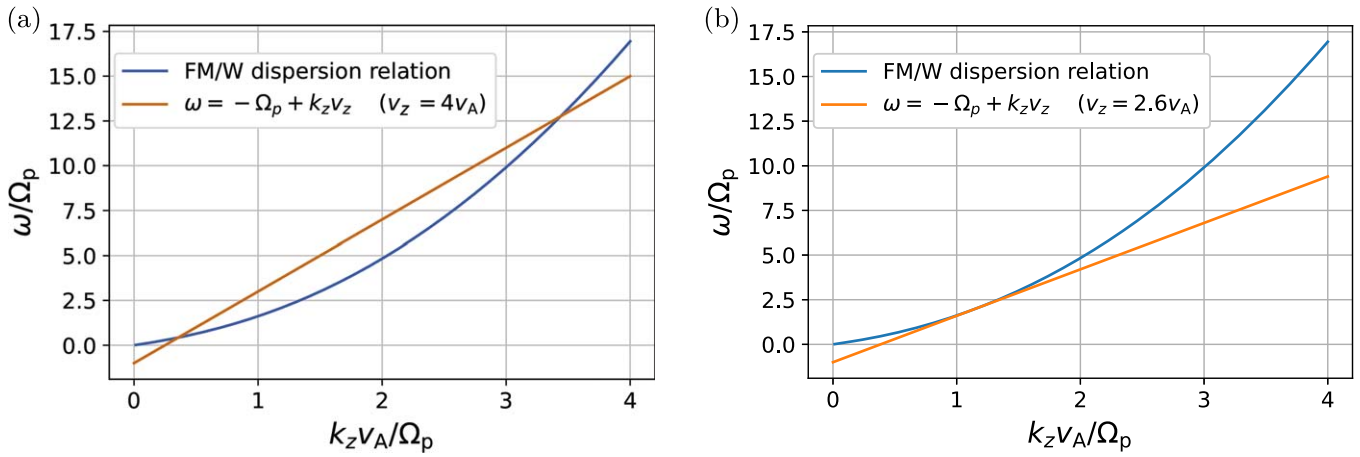


Figure 5. The cold-plasma FM/W dispersion relation (Equation (4)) and the wave−particle resonance condition for a proton beam ($b = 1$ in Equation (7)). Resonant wave–particle interactions can occur when both curves intersect. Panel (a) corresponds to protons with parallel velocity $v_z = 4v_A$. Panel (b) corresponds to protons with $v_z = 2.6v_A$, which is the minimum value of v_z for which protons can resonate with FM/W waves in the cold proton-electron plasma approximation.

determined by the requirement that, as the corkscrew travels past the $z = 0$ plane in the $+z$ direction, the electric field vector in the $z = 0$ plane undergoes right circularly polarized rotation. Because ions undergo left circularly polarized Larmor rotation, an ion that remains in the $z = 0$ plane (i.e., at $z = 0$ with v_z=0) does not resonate with an FM/W wave as it encounters a time-varying electric field. By contrast, if $v_z > \omega/k_z$ for some ion, then in the "parallel co-moving frame" for that ion (which moves at velocity v_z along $\boldsymbol{B}_0$), the electric field corkscrew appears to propagate in the $-z$ direction. If the ion then fulfills $\omega - k_z v_z = -\Omega$, in the parallel co-moving frame, the electric field vector appears constant, which enables the FM/W wave to resonate with the ion. When $n = -1$, the Doppler-shifted frequency $\omega - k_z v_z$ is negative, implying that $v_z > \omega/k_z$.

It follows from the foregoing discussion that we set

$$\Omega = b\Omega_p \tag{6}$$

in Equation (5), where $b = 1$ corresponds to proton beams. We then re-write Equation (5) as

$$y = -b + xu, \tag{7}$$

where

$$u = \frac{v_z}{v_A}. \tag{8}$$

The combinations of (x, y) that fulfill both Equations (7) and (2) gives the wavenumbers and frequencies at which FM/W waves resonantly interact with ions with parallel velocity v_z. Panel (a) of Figure 5 illustrates this condition for beam protons ($b = 1$ in Equation (7)) with $v_z = 4v_A$ and FM/W waves described by the cold-plasma dispersion relation. If we were to decrease v_z, then the slope of the resonance line (the solution of Equation (7)) would decrease, leaving the y-intercept of this line unchanged. Below a certain value of v_z, denoted by v_{min}, the resonance line no longer intersects the dispersion relation (as long as $0 < \omega \ll \Omega_e$). As a consequence, beam protons interact with slab FM/W waves only when $v_z \geqslant v_{min}$. When the FM/W waves are described using the cold-plasma dispersion relation, $v_{min} = 2.60v_A$. However, $v_{min} = 2.68v_A$ when $F(x)$ in Equation (4) is determined from the hot-plasma dispersion relation for a Maxwellian, single-temperature, proton-electron plasma with $\beta = 1$ using the PLUME code (Klein & Howes 2015), where β is the ratio of plasma pressure to magnetic pressure. Panel (b) of Figure 5 reproduces panel (a) but with $v_z = 2.6v_A$.

When an ion resonates with an FM/W wave at a particular resonant wavenumber and frequency, the ion diffuses along a contour in the $v_\parallel - v_\perp$ plane that corresponds to a constant ion kinetic energy in the reference frame that moves along $\boldsymbol{B}_0$ at the phase velocity ω/k_z of the wave (Stix 1992), the wave frame. Conservation of particle kinetic energy in the wave frame is a consequence of the fact that the electric and magnetic fields are constant in time in the wave frame. Faraday's Law then implies that $\nabla \times \boldsymbol{E} = 0$, so that the electric field in the wave frame can be written as the gradient of a potential Φ. The relative velocity between the wave frame and proton frame is parallel to $\boldsymbol{B}_0$. As a consequence, transforming from the proton frame to the wave frame does not lead to the appearance of a constant electric field. Because an ion's total energy $m(v')^2/2 + q\Phi$ in the wave frame is constant (where $\boldsymbol{v}'$ is the ion's velocity in the wave frame), $m(v')^2/2$ is effectively conserved. (For a different explanation in terms of wave quanta and energy and momentum conservation, see Stix 1992.)

Figure 6 illustrates this energy-conserving velocity-space diffusion for the wave−particle resonances illustrated in Figure 5(a), corresponding to beam protons with $v_z = 4v_A$. As illustrated in this figure, beam protons with $v_z = 4v_A$ can resonantly interact with FM/W waves at two different wavenumbers, one satisfying $k_z v_A/\Omega_p = 0.356$, and one satisfying $k_z v_A/\Omega_p = 3.44$, which we refer to as the low-k resonance and high-k resonance, respectively. In the case of the low-k resonance, the phase velocity ω/k_z of the resonant waves is $1.19v_A$. If we imagine that protons and FM/W waves interact only via the low-k resonance, then protons with $v_z = 4v_A$ diffuse along contours in the $v_\parallel - v_\perp$ plane that are locally tangent to semicircles centered at $v_\parallel = 1.19v_A$ and $v_\perp = 0$. This is illustrated by the solid-line diffusion contour in the lower-left plot of Figure 6. The entirety of the diffusion contour, however, is not semicircular, because the FM/W waves are dispersive. For example, as the particle's v_z changes during the diffusion, so would the phase speed of the resonant waves, and thus the local tangent that describes the diffusion path. The solid curve in the lower-left plot of Figure 6 shows a diffusion contour that, at each v_z, is locally tangent to a semicircle centered at $v_\perp = 0$ and $v_z = v_{phase}^{(low)}(v_z)$, where $v_{phase}^{(low)}(v_z)$ is the value of ω/k_z for the

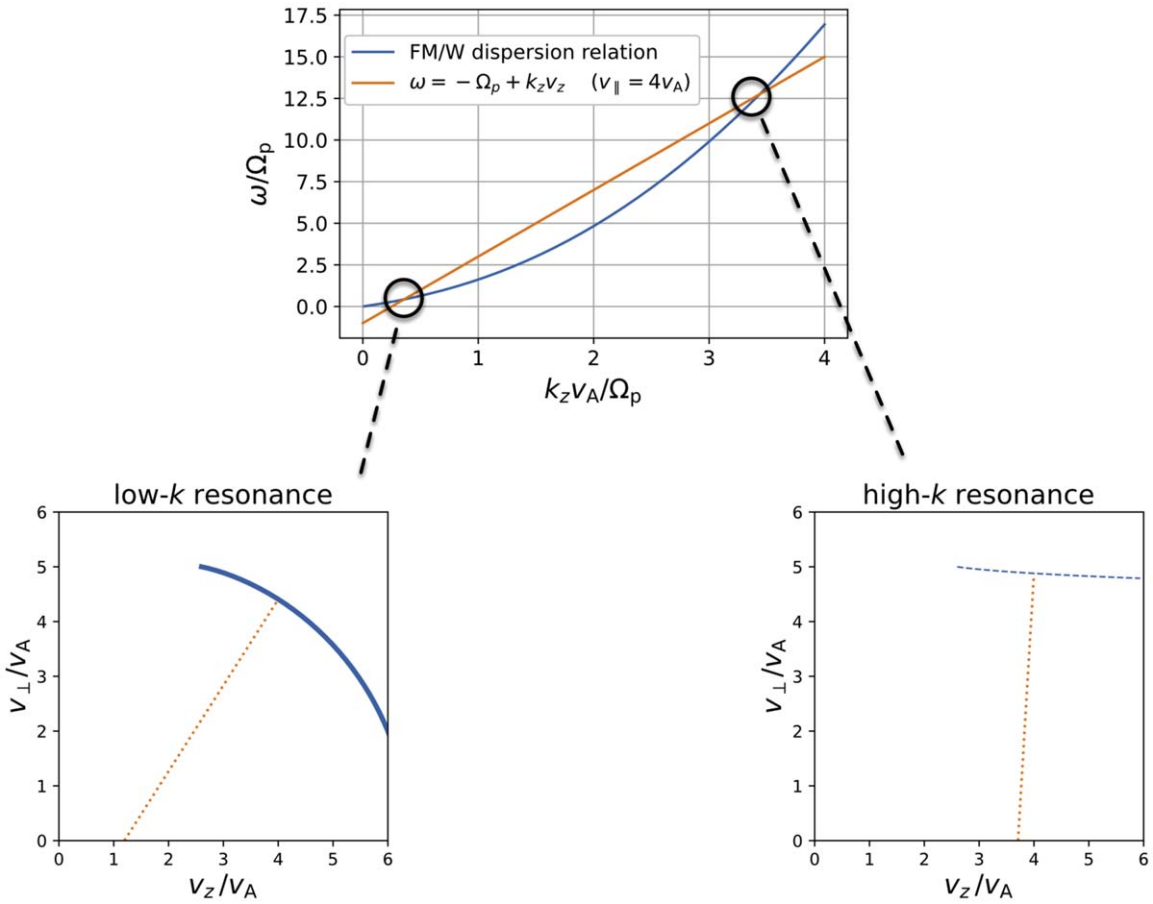


Figure 6. The top plot shows the FM/W dispersion relation (blue) intersecting with the $n = -1$ resonance curve (orange). The lower-left and lower-right panels display the diffusion path cases for ions to resonate with FM/W waves via the low-k and high-k resonance, respectively, mapped to the $(\frac{v_\perp}{v_A}, \frac{v_z}{v_A})$ plane.

FM/W waves that resonate with ions of a given v_z via the low-k resonance.

For the high-k resonance shown in Figure 6, ω/k_z is $3.71v_A$. If we imagine that ions and FM/W waves interact only via the high-k resonance, then an ion with $v_z = 4v_A$ interacting with FM/W waves via this high-k resonance diffuses in the $v_\parallel - v_\perp$ plane along a contour that is locally tangent to a semicircle centered at $v_z = 3.71v_A$ and $v_\perp = 0$. Like in the case of the low-k resonance, the phase speed of the resonant waves depends on v_z. The dashed line in the lower-right plot in Figure 6 shows a diffusion contour that, at each v_z, is locally tangent to a semicircle centered at $v_\perp = 0$ and $v_z = v_{\rm phase}^{\rm (high)}(v_z)$, where $v_{\rm phase}^{\rm (high)}(v_z)$ is the value of ω/k_z for the FM/W waves that resonate with ions of a given v_z via the high-k resonance.

If, as in the preceding paragraphs, we suppose that only one of the two resonances (either low-k or high-k) is active, then the velocity-space contours along which the particles diffuse $v_\perp(v_z)$ can be computed as follows. The line that connects an ion's velocity-space coordinates $(v_z,\ v_\perp)$ to the velocity-space coordinates $(v_{\rm phase}(v_z),\ 0)$ of the wave frame of the waves that resonate with that ion has a slope of $v_\perp/[v_z - v_{\rm phase}(v_z)]$, where $v_{\rm phase}(v_z)$ is either $v_{\rm phase}^{\rm (low)}$ or $v_{\rm phase}^{\rm (high)}$, depending on which of the two resonances is assumed to be active. This line is perpendicular to the diffusion contour described by the function $v_\perp(v_z)$, from which it follows that

$$\frac{dv_\perp}{dv_z} = \frac{v_{\rm phase}(v_z) - v_z}{v_\perp}. \tag{9}$$

(This point is nicely illustrated in Figure 2 of Isenberg & Lee 1996.) Equation (9) can be integrated to yield

$$\frac{v_\perp^2}{2} = -\frac{v_z^2}{2} + \int v_{\rm phase}(v_z)\mathrm{d}v_z + C, \tag{10}$$

where C is an integration constant representing an arbitrary offset (for simplicity, we set $C = 0$). Isenberg & Lee (1996) evaluated Equation (10) analytically for the low-k resonance using the cold-plasma dispersion relation in Equation (4), obtaining a parametric solution for $v_\perp(v_z)$ given in their Equations (14) and (15). Some examples of the resulting contours are shown in Figure 7(a), which also includes (numerical) solutions for the diffusion contours associated with the high-k resonance. Figure 7(b) shows the diffusion contours that result when $F(x)$ in Equation (2) is determined from numerical solutions to the hot-plasma dispersion relation for a Maxwellian, single-temperature, electron-proton plasma with $\beta = 1$ using the PLUME code (Klein & Howes 2015).

If a population of beam ions initiates with a distribution function $f(v_z,\ v_\perp)$ that extends to values of v_z exceeding $2.6v_A$, then the beam ions can resonantly interact with FM/W waves and diffuse along the contours pictured in Figure 7. Their

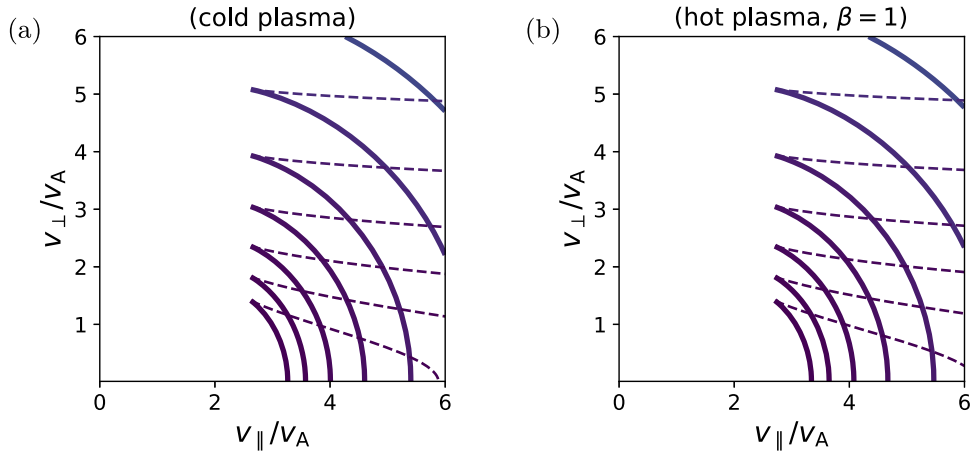


Figure 7. Velocity-space diffusion contours corresponding to the low-k resonance (solid lines) and high-k resonance (dashed lines). In panel (a), the FM/W waves obey the cold-plasma dispersion relation for a proton-electron plasma (Equation (4)). In panel (b), the FM/W waves obey the hot-plasma dispersion relation for a Maxwellian, single-temperature, proton-electron plasma with $\beta = 1$. The direction of the diffusion along these contours is determined by the condition that the diffusion occurs from larger to smaller values of $f(v_z, v_\perp)$.

diffusion direction (upward or downward) depends on the gradient of $f(v_z, v_\perp)$. The diffusion would go upward (downward) if, when traveling upward (downward) along the diffusion path, the value of $f(v_z, v_\perp)$ decreases (increases). For concreteness, we assume the former condition is true for $f(v_z, v_\perp)$.

Because the ions diffuse from regions of higher particle concentration to regions of lower particle concentration in velocity space, they will diffuse upward along the low-k resonance contours pictured in Figure 7 toward larger values of $v_\perp$. Although these ions experience an increase in $v_\perp$, they undergo parallel deceleration, and an ion's total kinetic energy decreases as it diffuses up along one of the low-k resonance contours. This net loss of energy is illustrated in panel (a) of Figure 8. The energy lost by the resonant ions is transferred to the resonant FM/W waves, causing them to grow. This process occurs on the quasilinear interaction timescale, which can be of order a few wave periods (Isenberg & Lee 1996) and drives the particles toward a state in which the instability ceases to grow (i.e., the marginally stable state where diffusion contours are referred to as "kinetic shells"; see, e.g., Isenberg et al. 2001).

For the FM/W waves in the cold-plasma approximation, the kinetic shells end when v_z drops to values of $\simeq 2.6 v_A$, below which the ions are unable to resonate with the FM/W waves. The level contours of such a marginally stable distribution have a "hammerhead" shape at $v_z \gtrsim 2.6 v_A$, similar to some of the ion distribution functions seen by PSP, as illustrated in panel (b) of Figure 8. This suggests that the hammerhead features in the observed VDFs are the result of proton beam driven instabilities of the parallel FM/W instability. For an initially Maxwellian beam, such an instability is only driven if the beam bulk speed in the proton bulk frame is greater than the parallel phase speed of the resonant wave (Verscharen & Chandran 2013).

In principle, the beam ions can also resonate with FM/W waves via the high-k resonance. Due to the condition of diffusion toward smaller values of $f(v_z, v_\perp)$, the diffusing ions in that range would typically gain energy in the interaction. This kinetic energy would be drained from the resonant FM/W waves, causing those waves to dampen. Because of this, we conjecture that the high-k resonance is not significantly activated by the beam distributions encountered by PSP, which justifies our neglect of this second resonance when computing the kinetic shells.

4. Conclusions and Future Work

In this paper, we present new PSP observations of proton VDFs in which the proton beam is strongly broadened perpendicular to the magnetic field over a narrow range of parallel velocities, leading to VDF level contours with a hammerhead shape. In Section 2, we quantify this extra asymmetry by approximating the proton VDF as the sum of three components: a core, a narrow field-aligned beam, and a broadened "hammerhead", as seen in Figure 1(a). These new complex VDFs were first observed during a 7 hr right-hand circularly polarized wave storm at the ion gyrofrequency scale displayed in Figures 1(b)–(e). We explored how different properties of the hammerhead population (fractional density, temperature anisotropy, and drift Alfvén Mach number) correlate with one another during a 7 hr interval of PSP's fourth perihelion encounter with the Sun. These initial results from the triple bi-Maxwellian SPAN-I VDF fitting during this event are shown in Figure 2, which suggest that the temperature anisotropy of the hammerhead population is the most consequential parameter. Future studies will use this diagnostic to produce a statistical characterization of the hammerhead occurrence rate as a function of various solar wind parameters, yielding insight on the nature of ion velocity-space diffusion as a solar wind heating mechanism.

The prevalence of the hammerhead features in the proton VDF is also coincident with the energy density of ion-scale waves that are right circularly polarized in the spacecraft frame. This is seen by observing the association of the enhancement of RH wave energy density in Figure 3(a) with the change in proton VDF fitting parameters displayed in Figures 3(b)−(d). It was again found that the increase in temperature anisotropy was most indicative of the presence of a hammerhead, as further illustrated by Figure 4. Since the solar wind Mach number during the 7 hr wave event was close to unity, the approximation of Doppler-shifted frequencies from the spacecraft to the plasma frame is nontrivial (see Bowen et al. 2020) and will be left for future work. A plasma dispersion analysis can be applied to the three-component fits to better examine the components of the proton VDF leading to wave growth and/or

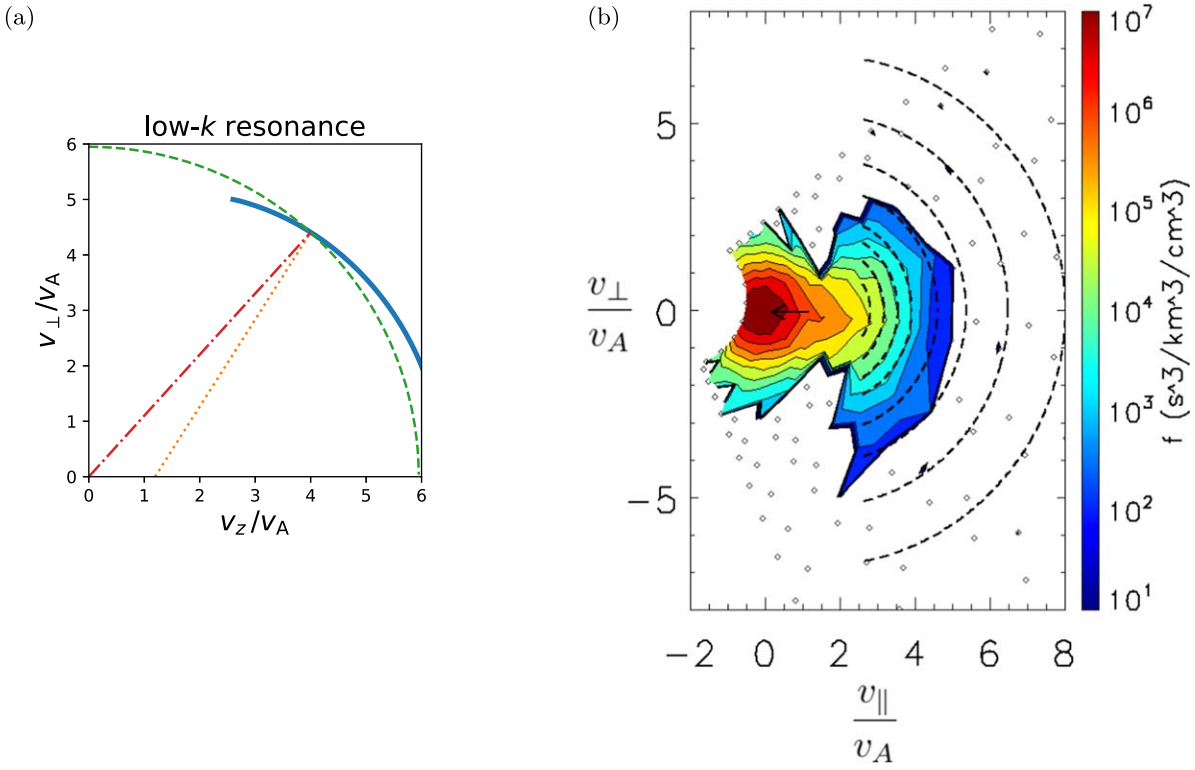


Figure 8. Panel (a): the solid line represents the same diffusion contour for the low-k resonance that was pictured in the lower-left plot of Figure 6, which is locally tangent to a semicircle centered on the velocity coordinates of FM/W waves that resonate with the ions at each different v_z. The dashed line is a semicircle of constant energy in the plasma rest frame, which is centered on the origin. As particles diffuse upward along the diffusion contour, their total kinetic energy decreases. Panel (b): example proton VDF in field-aligned plasma-frame coordinates, overplotted with dashed line low-k resonance contours when the FM/W waves are described using the cold-plasma approximation.

decay. A more comprehensive wave analysis can also be performed to better characterize the correlation between the observed ion-strahl diffusion and right-hand circularly polarized waves over multiple encounters. The results presented in Section 2 demonstrate a preliminary attempt at understanding the wave−particle energy transfer dynamics associated with the new asymmetries found in the proton VDFs.

In Section 3 we develop a theoretical model that explains the shape of these proton VDFs. This model is based on earlier work by Isenberg & Lee (1996) where beam protons cause right circularly polarized, parallel-propagating, FM/W waves to become unstable and grow. When a beam proton resonantly interacts with an FM/W wave, the proton's energy is conserved in the reference frame that propagates along the background magnetic field at the wave's phase velocity. This conservation law causes the protons to diffuse along a particular set of contours in the $v_z - v_\perp$ plane (where v_z and $v_\perp$ are velocity components parallel and perpendicular to $\boldsymbol{B}_0$) that can be computed based on the FM/W dispersion relation. Beam protons whose velocities are initially nearly aligned with $\boldsymbol{B}_0$ diffuse along these contours to smaller values of v_z and larger values of $v_\perp$. The net effect of this parallel deceleration and perpendicular thermalization is to reduce the protons' kinetic energies (Figure 8(a)). The energy lost by the protons is transferred to the FM/W waves, which causes the waves to grow. Velocity-space diffusion causes the proton distribution function $f(v_z, v_\perp)$ to become constant along the aforementioned velocity-space diffusion contours, causing the plasma to become marginally stable to the growth of FM/W waves. The resulting constant-f lines, or "kinetic shells" (Isenberg et al. 2001), is consistent with the constant-f lines in the hammerhead portion of the ion VDFs observed by PSP that are shown in Section 2. This agreement, along with the association in the PSP observations between hammerhead features and right circularly polarized ion-scale waves, suggest that the hammerhead VDFs seen by PSP indeed result from resonant interactions between beam protons and FM/W waves. We speculate that this process is more intense in the near-Sun environment, which is possibly why we do not observe the hammerhead features in VDFs measured at larger distances. The heliographic position of PSP, along with the SPAN-I field-of-view limitations will also be considered in future investigations.

The primary goal of this paper was to report the novel wave−particle PSP observations and to use linear theory to provide an intuitive explanation of their significance. Given the highly non-Maxwellian nature of the observed proton VDFs, numerical simulations will be needed to understand the dynamics of these distributions. Here, we used linear theory to estimate growth rates, dominant modes, and implied phase speeds. We acknowledge that a more sophisticated treatment could include additional nonlinear effects, such as finite-width trapping, as described in Karimabadi et al. (1992) and applied to pick-up ions at Comet Halley in Karimabadi et al. (1994). However, such effects are beyond the scope of this paper and our observations report from a different heliospheric context.

These new PSP observations raise new inquiries regarding the contribution of these powerful ion beams to the solar wind energy flux and the ongoing heating of the near-Sun solar wind. The source of the initial beam of field-aligned particles that eventually diffuses into the hammerhead region of velocity space also remains elusive. As PSP flies closer to the Sun,

however, the ion VDFs will become more favorable to the SPAN-I field of view. More reliable measurements will lead to a better characterization of their complex shape as a function of plasma parameters of interest such as plasma β, general heliographic position, angular proximity to the heliospheric current sheet, and distance from magnetic topological changes. Thus, future PSP observations will likely provide answers to these important questions about the dynamics and thermodynamics of the inner heliosphere.

The SWEAP Investigation is supported by the PSP mission under NASA contract NNN06AA01C. K.G.K. is supported by NASA ECIP grant 80NSSC19K0912. D.V. is supported by STFC Ernest Rutherford Fellowship ST/P003826/1 and STFC Consolidated Grant ST/S000240/1. B.L.A. acknowledges NASA contract NNG10EK25C.

ORCID iDs

J. L. Verniero https://orcid.org/0000-0003-1138-652X
B. D. G. Chandran https://orcid.org/0000-0003-4177-3328
D. E. Larson https://orcid.org/0000-0001-5030-6030
K. Paulson https://orcid.org/0000-0002-5699-090X
B. L. Alterman https://orcid.org/0000-0001-6673-3432
S. D. Bale https://orcid.org/0000-0002-1989-3596
J. W. Bonnell https://orcid.org/0000-0002-0675-7907
T. A. Bowen https://orcid.org/0000-0002-4625-3332
T. Dudok de Wit https://orcid.org/0000-0002-4401-0943
J. C. Kasper https://orcid.org/0000-0002-7077-930X
K. G. Klein https://orcid.org/0000-0001-6038-1923
E. Lichko https://orcid.org/0000-0003-1945-8460
R. Livi https://orcid.org/0000-0002-0396-0547
M. D. McManus https://orcid.org/0000-0001-6077-4145
D. Verscharen https://orcid.org/0000-0002-0497-1096
P. L. Whittlesey https://orcid.org/0000-0002-7287-5098

References

Alterman, B. L., Kasper, J. C., Stevens, M. L., & Koval, A. 2018, ApJ, 864, 112
Bale, S. D., Badman, S. T., Bonnell, J. W., et al. 2019, Natur, 576, 237
Bale, S. D., Goetz, K., Harvey, P. R., et al. 2016, SSRv, 204, 49
Bowen, T. A., Bale, S. D., Bonnell, J. W., et al. 2020, ApJ, 899, 74
Bowen, T. A., Mallet, A., Huang, J., et al. 2020a, ApJS, 246, 66
Case, A. W., Kasper, J. C., Stevens, M. L., et al. 2020, ApJS, 246, 43
Daughton, W., & Gary, P. S. 1998, JGR, 103, 20613
Feldman, W. C., Asbridge, J. R., Bame, S. J., & Montgomery, M. D. 1973, JGR, 78, 2017
Feldman, W. C., Asbridge, J. R., Bame, S. J., & Montgomery, M. D. 1974, RvGSP, 12, 715
Fox, N. J., Velli, M. C., Bale, S. D., et al. 2016, SSRv, 204, 7
Gary, S. P., Yin, L., Winske, D., & Reisenfeld, D. B. 2000, GeoRL, 27, 1355
Hu, Y. Q., & Habbal, S. R. 1999, JGR, 104, 17045
Isenberg, P. A., & Lee, M. A. 1996, JGRA, 101, 11055
Isenberg, P. A., Lee, M. A., & Hollweg, J. V. 2001, JGR, 106, 5649
Karimabadi, H., Krauss-Varban, D., Omidi, N., Fuselier, S. A., & Neugebauer, M. 1994, JGR, 99, 21541
Karimabadi, H., Krauss-Varban, D., & Terasawa, T. 1992, JGR, 97, 13853
Kasper, J. C., Abiad, R., Austin, G., et al. 2016, SSRv, 204, 131
Kasper, J. C., Lazarus, A. J., Steinberg, J. T., Ogilvie, K. W., & Szabo, A. 2006, JGRA, 111, A03105
Klein, K. G., Alterman, B. L., Stevens, M. L., Vech, D., & Kasper, J. C. 2018, PhRvL, 120, 205102
Klein, K. G., & Howes, G. G. 2015, PhPl, 22, 032903
Klein, K. G., Verniero, J. L., Alterman, B., et al. 2021, ApJ, 909, 7
Levenberg, K. 1944, QApMa, 2, 164
Livi, R., Larson, D. E., Kasper, J. C., et al. 2021, ApJ, submitted
Maneva, Y. G., Viñas, A. F., & Ofman, L. 2013, JGR, 118, 2842
Marquardt, D. W. 1963, J. Soc. Ind. Appl. Math., 11, 431
Marsch, E. 2006, LRSP, 3, 1
Marsch, E., & Livi, S. 1987, JGR, 92, 7263
Marsch, E., Schwenn, R., Rosenbauer, H., et al. 1982, JGR, 87, 52
Neugebauer, M., Goldstein, B. E., Smith, E. J., & Feldman, W. C. 1996, JGR, 101, 17047
Podesta, J. J., & Gary, S. P. 2011, ApJ, 734, 15
Steinberg, J. T., Lazarus, A. J., Ogilvie, K. W., Lepping, R., & Byrnes, J. 1996, GeoRL, 23, 1183
Stix, T. H. 1992, Waves in Plasmas (New York: American Institute of Physics)
Torrence, C., & Compo, G. P. 1998, BAMS, 79, 61
Tsurutani, B. T., & Lakhina, G. S. 1997, RvGeo, 35, 491
Ďurovcová, T., Šafránková, J., & Němeček, Z. 2019, SoPh, 294, 97
Verniero, J. L., Larson, D. E., Livi, R., et al. 2020, ApJS, 248, 5
Verscharen, D., Bourouaine, S., Chand Ran, B. D. G., et al. 2013a, ApJ, 773, 163
Verscharen, D., Bourouaine, S., Chandran, B. D. G., & Maruca, B. A. 2013b, ApJ, 773, 8
Verscharen, D., & Chandran, B. D. G. 2013, ApJ, 764, 88
Verscharen, D., Chandran, B. D. G., Bourouaine, S., & Hollweg, J. V. 2015, ApJ, 806, 157
Whittlesey, P. L., Larson, D. E., Kasper, J. C., et al. 2020, ApJS, 246, 74